

Maximising transferred power and preserving zero voltage switching in grid to vehicle and vehicle to grid modes of a wireless charging system

Jean-Paul Ferrieux¹, Gatién Kwimang¹, Gérard Meunier¹, Benoît Sarrazin¹, Alexis Derby¹, Teymoor Ghanbari², Ebrahim Farjah² ✉

¹Université Grenoble Alpes, CNRS, Grenoble INP, G2Elab, 38000 Grenoble, France

²Department of ECE, Shiraz University, Shiraz, Iran

✉ E-mail: farjah@shirazu.ac.ir

Abstract: Modelling of a wireless charging system for an electrical vehicle is one of the main challenges to control the system, optimally. Considering a suitable integrated model for both the vehicle and stationary sides is essential to guarantee the maximum power transfer in these systems. This study presents an analytical model of an inductive contactless charger, used for controlling the vehicle side of the system to transfer charging power and regenerative (vehicle to grid) power as high as possible. First, the system parameters are set based on the derived analytical model, then the settings are readjusted by a finite-element model as a fine tuning. The system is controlled in a way that soft switching in both the charging and regenerative modes is guaranteed. The under study system has 20 kW power with an inter-coil distance between 14 and 21 cm, and a bidirectional converter with series–series resonance compensation. The system is assessed in detail theoretically and the results are confirmed using some experiments carried out on a prototype in the same rating.

1 Introduction

Electric vehicles (EVs) are promising alternatives for future transportation, aimed to alleviate environmental and fossil fuel concerns, realising high-performance refuelling systems is one of the main targets of EVs industry [1]. Broadly, these systems are classified as plug-in and contactless technologies. From the plug-in technologies, the parking lots, fast charging stations, and battery swapping stations can be mentioned. The contactless refuelling systems are divided into static and dynamic technologies [2, 3]. Although the plug-in charging systems have been widely developed and commercialised, the contactless ones need more investigations to overcome their challenges [1]. The plug-in charging systems have some drawbacks such as limited mileage per charge, vulnerability to weather conditions and vandalism, and the hazard of charging cables, which are aimed to be solved in the contactless systems [4–6].

Among the contactless charging systems, static ones are the most addressed because they face to fewer challenges in practice. However, there are many technical issues, which should be rectified in order to commercialise this technology [4, 5]. From the technical perspective, maximising transferred power to the EVs in such a complicated system is critical. Safety issues like field intrusions and electromagnetic field emissions, the need of desirable efficiency and interoperability, and required communication links are among the main causes of the system complexity [7–9].

An efficient control strategy is needed to guarantee the maximum transferred power and efficiency of the system in different conditions. To this end, one can employ a secondary-side (vehicle side) controller or a primary-side (ground side) one [10]. In general, the secondary-side controllers are preferred due to the simplicity of the system and the required communication link [10]. This is because a secondary-side controller is considered for the under-studied system in this work, as well.

Many research studies have been assigned to the secondary-side control of Wireless Power Transfer (WPT) systems from different aspects, such as the maximum efficiency control, the maximum transferred power control, and approaching to both these aspects

[10–15]. The key point of realising a desirable secondary-side control with any target is the availability of a suitable model of the system. Using this model, one can derive the best setting for the controller's parameters to follow different functions. Considering the governed conditions on the system, not only a robust simple model with low computational burden is required, but also accuracy of the model is in high degree of importance.

In this paper, an efficient controller is proposed to maximise transferred powers in grid to vehicle (G2V) and vehicle to grid (V2G) modes, while zero voltage switching (ZVS) is guaranteed in both the modes to fulfil the maximum efficiency of the system. An analytical analysis for a typical wireless charging system is presented. Based on the analysis, a simple analytical model for the system is derived, by which one can calculate the initial settings of the system's parameters. Since WPT systems have considerable leakage inductance in general, they cannot be modelled by the analytical model, accurately. Therefore, it is accurately modelled using the finite-element method (FEM) in the next step. Output results of the analytical model are used in an FEM-based analysis carried out by 3D FEM software FLUX. Using the FEM results, the optimal sizing and specifications of the coupler (dimensions and number of turns) are determined. The characterisation confirms the inductive model for calculating the resonances.

The main contribution of this work is the proposed controller and having ZVS in both the modes through the strategy of initial setting and fine tuning of the system's parameters.

The studied system will be limited to DC–DC conversion through a magnetic coupler without contact in medium frequency. The selected specifications are partially adopted to SAE standard J-2954 [16]; in particular, in order to meet the intermediate class Z2 of this standard. The power is supplied continuously from the charging terminal, while the secondary delivers continuous power directly/indirectly to the battery.

The considered system has a 20 kW magnetic coupler, an inter-coil distance between 14 and 21 cm, and a bidirectional converter with series–series resonance compensation. Firstly, a simplified coupler sizing method is developed and then the conversion system is analysed in order to have a bidirectional power system allowing the exchange of energy in G2V and V2G modes.

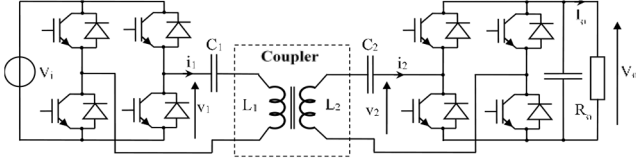


Fig. 1 Schematic of a series-series resonant DC-DC converter

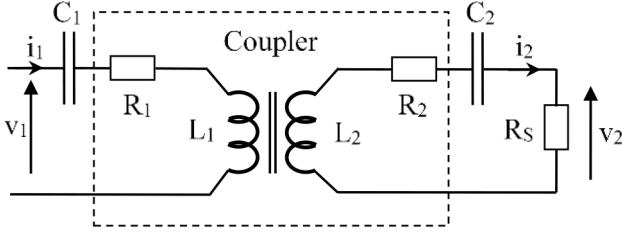


Fig. 2 First-order harmonic equivalent circuit

Analytical analysis of the system is presented in detail and an analytical model for setting the control parameters is derived. Also, a prototype system in the same rating has been fabricated in the laboratory. Some experiments have also been carried out to assess the model. The theoretical results agree well with the experimental ones, which confirm the accuracy of the model.

2 Structure of the energy conversion

In this section, the structure of the considered energy conversion system is discussed from some aspects.

2.1 Selection of the conversion structure

The DC-DC conversion structure must transfer the power at medium frequency through a large air-gap coupler. This coupler, as a 'pancake' shape, has the particularity of having significant leaks and a low magnetising inductance. Then, it is necessary to compensate the required reactive power. It has shown that compensation by series capacitors in primary and secondary is a good remedy. Compared to the series or series-parallel resonances, this compensation has a better efficiency and a lower sensitivity to the positioning, since the resonance takes place with the self-inductances, independent of the mutual inductance.

The selected topology is shown in Fig. 1, composed of two bridge inverters. This structure like a dual active bridge (DAB) with resonance has several control variables:

- Duty cycles of each inverter (noted α_1, α_2) that will control the effective values of voltages v_1, v_2 .
- Phase shift between the inverters, noted ϕ , will provide power control and directionality.
- Frequency, close to the resonance, will guarantee the desired phase shift.

In the charging mode (transfer of energy to the battery), in order to simplify the communication between the primary part (on the ground) and the secondary (vehicle), the control will be carried out with the primary bridge by action on the frequency and duty cycle. So, the secondary bridge will then be uncontrolled (diode operation). The case of energy transfer from the battery to the grid will be discussed in Section 6.

2.2 First harmonic study

The study could be done for a simplified first-order harmonic. Indeed, the presence of the resonant circuits induces quasi-sinusoidal currents, justifying the approximation of the first harmonic method.

In the simplified diagram of Fig. 2, voltages v_1 and v_2 represent the fundamental terms defined by effective value:

$$V_{1rms} = \frac{4}{\pi\sqrt{2}} V_i \sin(\alpha_i \pi) \quad (1)$$

$$V_{2rms} = \frac{4}{\pi\sqrt{2}} V_o \quad (2)$$

where V_i is the input voltage and V_o the output one. So

$$R_s = \frac{8}{\pi^2} R_o \quad (3)$$

$$I_o = \frac{2\sqrt{2}}{\pi} I_{2rms} \quad (4)$$

From the equations of the coupler, one could express the following formulas between the principal quantities for any frequency:

$$\underline{V}_1 = jL_1\omega\underline{I}_1 + R_1\underline{I}_1 + \frac{\underline{I}_1}{jC_1\omega} - jM\omega\underline{I}_2 \quad (5)$$

$$jM\omega\underline{I}_1 - jL_2\omega\underline{I}_2 = (R_s + R_2)\underline{I}_2 + \frac{\underline{I}_2}{jL_2\omega} \quad (6)$$

with these two expressions, currents \underline{I}_1 and \underline{I}_2 could be expressed as:

$$\underline{I}_1 = \frac{\underline{V}_1((R_s + R_2) + jL_2\omega + (1/jC_2\omega))}{(M\omega)^2 + (R_1 + jL_1\omega + (1/jC_1\omega))((R_s + R_2) + jL_2\omega + (1/jC_2\omega))} \quad (7)$$

$$\underline{I}_2 = \frac{jM\omega\underline{V}_1}{(M\omega)^2 + (R_1 + jL_1\omega + (1/jC_1\omega))((R_s + R_2) + jL_2\omega + (1/jC_2\omega))} \quad (8)$$

In the first step, in order to show the behaviour of the converter, this expression could be simplified considering resistances of the coils equal to zero and by being placed with the resonance frequency defined by

$$F_R = \frac{1}{2\pi\sqrt{L_1C_1}} = \frac{1}{2\pi\sqrt{L_2C_2}} \quad (9)$$

The expression of the secondary current I_2 in (8) is simplified and the current source behaviour of the structure is highlighted:

$$\underline{I}_2 = \frac{j\underline{V}_1}{M\omega_R}$$

In which

$$I_o = \frac{8}{\pi^2} \frac{V_i \sin(\alpha_i \pi)}{M\omega_R} \quad (10)$$

At resonance, the load current is therefore independent of the load voltage and can be controlled by the inverter. One can note from now on the important role of the mutual inductance, thus of the coupling. In the same way, the primary current could be represented by

$$\underline{I}_1 = \frac{\underline{V}_2}{jM\omega_R} \quad (11)$$

Equation (11) shows that the primary current depends only on the output voltage. In the case of a substantially constant voltage

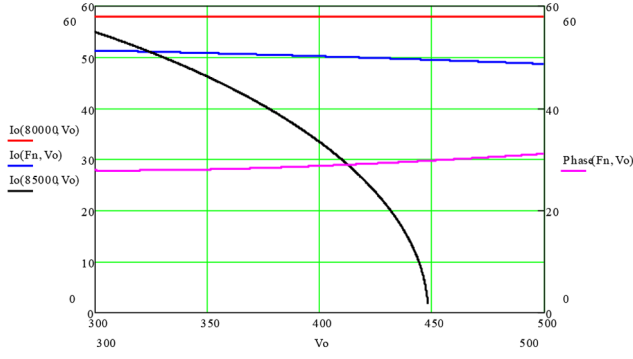


Fig. 3 Output characteristics and primary phase

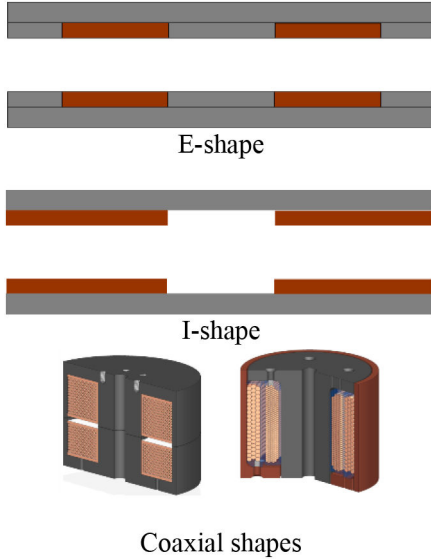


Fig. 4 Some shapes for the magnetic system

battery charging, it will be necessary to act on the output inverter bridge to minimise this variable power current.

Using (10) and (11), it is possible to evaluate the voltage stresses on the resonance capacitors that can be expressed as a function of the coupling coefficient k :

$$k = \frac{M}{\sqrt{L_1 L_2}} = \frac{1}{m} \frac{M}{L_1} = m \frac{M}{L_2} \quad (12)$$

$$V_{C1rms} = \frac{I_{1rms}}{C_1 \omega_R} = \frac{V_{2rms}}{C_1 M \omega_R^2} = \frac{1}{k} \frac{4V_o}{m\pi\sqrt{2}} \quad (13)$$

$$V_{C2rms} = \frac{I_{2rms}}{C_2 \omega_R} = \frac{V_{1rms}}{C_2 M \omega_R^2} = \frac{1}{k} \frac{4mV_i \sin(\alpha_1 \pi)}{\pi\sqrt{2}} \quad (14)$$

in which the transformation ratio $m = N_2/N_1$. These two formulas, valid only at resonance, show that the withstanding voltage is inversely proportional to the coupling coefficient and can therefore take high values for large gaps.

2.3 Selection of the conversion structure

The previous approach for the resonance frequency is insufficient since it is difficult to tune them perfectly. Indeed, the uncertainties on the values of the compensation capacitors and the positioning will make this adjustment impossible. In addition, the action on the frequency will be necessary to guarantee a minimum phase output of the inverter to ensure the proper switching mode.

In order to express the charging current as a function of the output voltage and the other control parameters, (8) with $R_1 = R_2 = 0$ is used and considering

$$Z_1 = L_1 \omega - \frac{1}{C_1 \omega} \text{ and } Z_2 = L_2 \omega - \frac{1}{C_2 \omega}$$

one could obtain

$$\underline{V}_1 = \frac{Z_1 V_2}{M \omega} + j \left(\frac{Z_1 Z_2}{M \omega} - M \omega \right) \underline{I}_2 \quad (15)$$

One can notice that v_2 and i_2 are in the phase, consequence of the resistive behaviour of the output rectifier. Using relations (1), (2) and (4), one can deduce a direct expression of the load current (I_o) as a function of the voltage (V_o) and frequency as:

$$I_o = \frac{8}{\pi^2} \frac{\sqrt{(M \omega V_i \sin(\alpha_1 \pi))^2 - (Z_1 V_o)^2}}{|Z_1 Z_2 - (M \omega)^2|} \quad (16)$$

These charging characteristics are shown in Fig. 3 for three frequencies: the resonance frequency (80 kHz, current generator), the nominal frequency F_n of 81.7 kHz to obtain 20 kW at 400 V, and a higher frequency (85 kHz) limiting the power.

Operation beyond the resonance frequency ensures the ZVS mode for the inverter. This requires an inductive impedance seen by the inverter that can be expressed from (7):

$$\phi_1 = \arg\left(\frac{V_1}{I_1}\right) = \arg\left(\frac{(M \omega)^2 + j Z_1 (R_s + j Z_2)}{R_s + j Z_2}\right) \quad (17)$$

This phase remains positive and its value is about 30° for the chosen nominal frequency. To guarantee a fast switching with the snubber capacitors, it is necessary to maintain a minimum phase; therefore, a minimum switched current is needed. This phase is the order of 20° for snubber capacitors of 3.3 nF (switching time lower than 750 ns at nominal power). The equations of the converter will be exploited for its design once the characteristics of the coupler are known.

3 Modelling and design of the coupler

3.1 Transmissible power for a series-series compensation

Proper design of a high air-gap coupler is a difficult task compared to that of a conventional transformer. On the one hand, there are no standard magnetic cores; on the other hand, the weak coupling imposes to reconsider the principle of dimensioning. The knowledge of the mutual inductance (M) and coupling coefficient (k) remains a key point for this sizing process. Moreover, the shape of the magnetic system can be chosen as planar E-shapes or simply I-shaped as shown in Fig. 4. Coaxial shapes can also be chosen in the case of transferring energy to a rotating part, as shown in Fig. 4 [4].

A first pre-designing approach will be carried out on the basis of the equivalent scheme of Fig. 2, neglecting the losses (with $R_1, R_2 = 0$) and considering that it operates at the resonant frequency. Power P_o that is aimed to transmit is expressed by

$$P_o = V_1 I_1 \text{ in which } I_1 = \frac{P_o}{V_1}$$

With a unity power factor in the vicinity of the resonance:

$$P_o = R_o I_o^2 = R_s I_2^2 \text{ in which } I_2 = \sqrt{\frac{P_o}{R_s}}$$

By referring to relation (10), we can express the required mutual inductance as

$$M \omega_R = \frac{V_1}{I_2} = V_1 \sqrt{\frac{R_s}{P_o}} \quad (18)$$

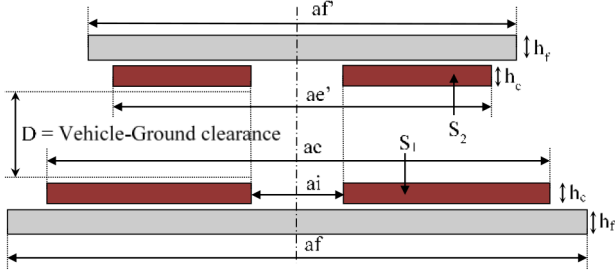


Fig. 5 Coupler cross-section

If M_u stands for the mutual inductance of a turn, such that $M = N_1 N_2 M_u$, we obtain

$$N_1 N_2 = \frac{V_1 \sqrt{R_S / P_o}}{M_u \omega_R} \quad (19)$$

Moreover, the primary and secondary ampere-turns are expressed by

$$N_1 I_1 = \frac{N_1 P_o}{V_1} \text{ and } N_2 I_2 = \frac{V_1}{N_1 M_u \omega_R}$$

The primary (J_1) and secondary (J_2) current densities are expressed as a function of turn number, the expansion coefficient λ and the sections of the primary (S_1) and secondary (S_2) coils (defined in Fig. 4):

$$J_1 = \frac{N_1 I_1}{\lambda S_1} \text{ and } J_2 = \frac{N_2 I_2}{\lambda S_2}$$

The number of turns can now be determined by seeking to minimise the Joule effect's own losses. These losses are expressed by

$$P_J = \rho \lambda (V_{w1} J_1^2 + V_{w2} J_2^2)$$

with V_{w1} and V_{w2} being the volumes of the windings and ρ the resistivity of the conductor. Winding volumes are calculated according to $V_{w1} = (ae^2 - ai^2)h_c$ and $V_{w2} = (ae'^2 - ai'^2)h_c$.

These losses can be expressed according to the number of the primary turns:

$$P_J = \rho \lambda \left(N_1^2 \frac{V_{w1} P_o^2}{\lambda^2 S_1^2 V_1^2} + \frac{1}{N_1^2} \frac{V_{w2} V_1^2}{\lambda^2 S_2^2 M_u^2 \omega_R^2} \right)$$

The minimisation of these losses makes it possible to determine the number of turns:

$$N_1 = \frac{V_1 \sqrt{q_s q_v}^{-1/4}}{\sqrt{M_u \omega_R P_o}} \quad (20)$$

defining $q_s = (S_1/S_2)$ and $q_v = (V_{w1}/V_{w2})$. Equation (19) allows one to deduce N_2 as follows:

$$N_2 = \frac{q_v^{1/4}}{\sqrt{q_s}} \sqrt{\frac{R_S}{M_u \omega}} \quad (21)$$

The transmittable power P_o under these conditions can be deduced from the current density J_1 and relation (20). So, considering J_1 as follows:

$$J_1 = \frac{N_1 I_1}{\lambda S_1} = \frac{N_1 P_o}{\lambda S_1 V_1} = \frac{V_1 \sqrt{q_s P_o q_v}^{-1/4}}{\sqrt{M_u \omega_R P_o} \lambda S_1 V_1}$$

One can obtain

$$P_o = \lambda^2 S_1 S_2 M_u \omega_R J_1^2 \sqrt{q_v} \quad (22)$$

This relation shows the need for maximising the coupling through the unitary mutual M_u . Although this remains as the difficulty in evaluating this unitary mutual, it is dependent on the winding sections and their shape. Moreover, the frequency is an important parameter which will increase the transmittable power to given winding sections, like for conventional transformers. Current density and frequency will be two important parameters for optimising the system.

3.2 Determining mutual unitary

Finite-element simulations are necessary to calculate the unitary mutual as a function of dimensions. A prior optimisation process has shown that it is preferable to have a 'spread' coil of low height. The simulations are performed in magnetostatics using Altair-Flux™ software in three dimensions according to the geometry shown in Fig. 5.

In practice, the resolutions were carried out with about 200,000 tetrahedral elements of order 1 (four nodes per element which correspond to 40,000 nodes, because each node shares between many elements) and of order 2 (ten nodes per element). Order 1 and Order 2 give the same result.

The inductor (the primary, ground part) has a square winding of internal dimensions: $ai = 100$ mm and external: ae variable, which will be determined by the power to be transmitted.

The armature (secondary, onboard part) has an external dimension such that $ae' = ae - 200$ mm, ensuring that the secondary remains face to face with the primary according to the positioning tolerance (± 100 mm, maximum tolerance of the standard for lateral positioning [4]).

The other dimensions are as follows:

- Thickness of the magnetic circuit: $h_f = 10$ mm, value resulting from an optimisation process.
- Thickness of the winding: $h_c = 9$ mm (height of the Litz wire).
- Magnetic circuit width (ferrite), primary and secondary: $af = 1.2ae$ and $af' = 1.2ae'$. The material has a relative permeability of 2300.

The simulation was performed for an inter-coil distance (D) between 14 and 21 cm (intermediate range Z2 of the standard). This dimension corresponds to the ground clearance of the vehicle. Nevertheless, the standard stipulates that the ground portion may exceed 70 mm; as a result, our simulation will cover the largest Z3 range (17–25 cm). Finally, it was taken into account a protective covering of 5 mm on each side of each coil in the simulations. The first simulation was performed with large radius of curvature, knowing that a small radius of curvature will be necessary to facilitate the placement of the Litz wire.

The simulation results are plotted versus size of the primary winding (ae) for the extreme values of the inter-coil distance D . Fig. 6a shows the mutual inductance in nH, whereas Fig. 6b represents the self-inductances.

4 Design and fabrication of the coupler

4.1 Pre-designing

The coupler will be designed for the most restrictive distance D (21 cm, simulated with 22 cm) and for the power of 20 kW. The transferable power is estimated by formula (22) considering the dimensions of Fig. 5 and an expansion coefficient of $\lambda = 0.26$. This coefficient takes into account that of the Litz wire (~ 0.43) and the inter-turn spacing. The other parameters are as follows:

- The nominal operating frequency of 85 kHz imposed by the standard ($81.38 < F < 90$ kHz).
- The primary current density is chosen at a low value (< 1.5 A/mm²) in order to limit proximity losses. This will lead to the choice of a Litz wire in the order of 25 mm².

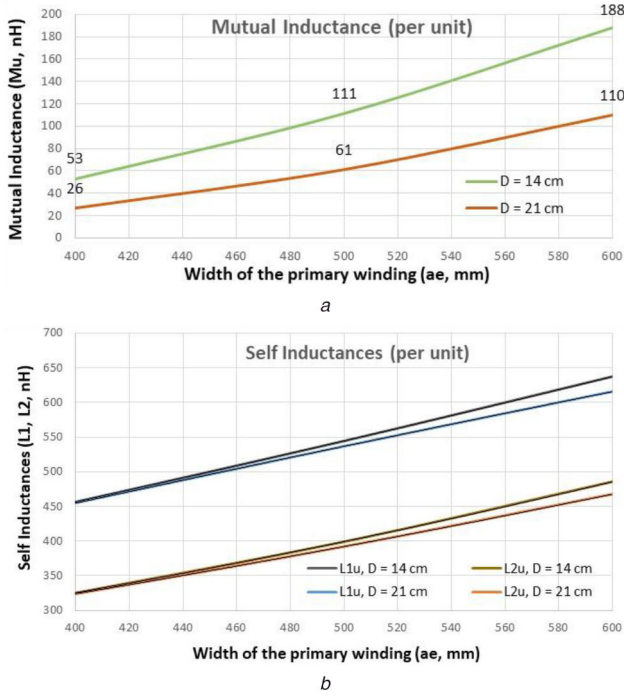


Fig. 6 Simulation results for different inductances
(a) Simulation of the mutual inductance (per number of turns), M_u ; (b) Simulation of the self-inductances (per number of turns), L_1, L_2

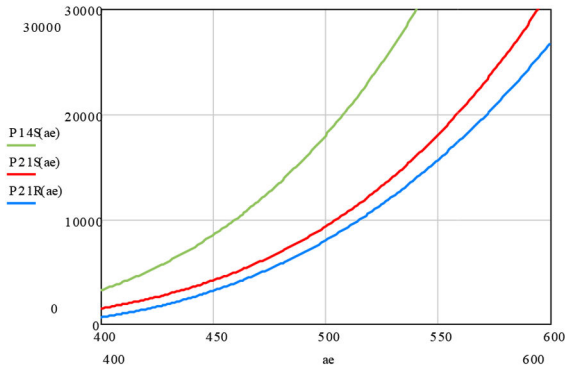


Fig. 7 Transferable power (P14S: square design, $D = 14$ cm; P21S: square design, $D = 21$ cm; P21R: round design, $D = 21$ cm)

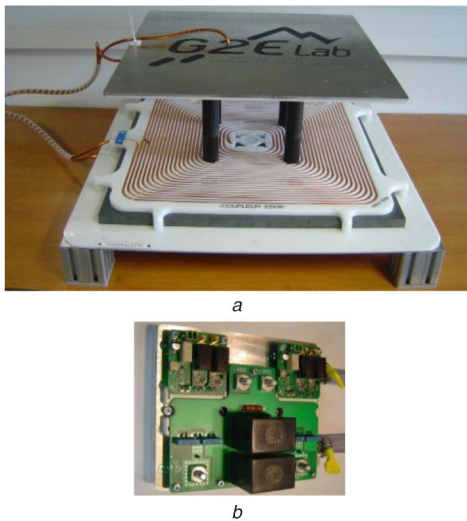


Fig. 8 Photos of the fabricated wireless charger
(a) Fabricated coupler, (b) Fabricated primary inverter

The transferable power is shown in Fig. 7 depending on dimensions of the primary coil for three configurations:

- square geometry, inter-coil distance of 14 cm,
- square geometry, inter-coil distance of 21 cm,
- round geometry, inter-coil distance of 21 cm, obtained results are about 30% worse than those of square windings. We will therefore retain the square geometry.

In accordance with this pre-design, a primary winding of 560 mm side was finally adopted.

4.2 Coupler fabrication

Based on the dimensions developed in Section 3, the turn numbers are set in $N_1 = 23$ and $N_2 = 12$ for a 21 cm inter-coil distance. The practical embodiment of the support makes it possible to add or remove a turn on each winding. From these numbers of turns, it is possible to determine the current densities by using relations defined in Section 3.1: 1.46 A/mm² in the primary and 2.2 A/mm² in the secondary. These densities are different considering the difference in the volume of the windings, which leads to the following conductor sections: 23.8 mm² (primary) and 26.3 mm² (secondary).

In practice, as the conductor sections are similar, the primary and secondary windings were made with the same Litz wire (3180 strands of 0.1 mm or 25 mm²) and were housed on plastic supports (POMc) and then transferred to ferrite magnetic circuits (SP 30-28-93, material 3C90) of external dimensions 660 × 651 mm (primary) and 465 × 420 mm (secondary) (Fig. 8a). Two aluminium plates with 5 mm thickness were placed outside the magnetic circuits to improve the shielding. These plates have external dimensions 800 × 800 mm (primary) and 600 × 600 mm (secondary).

4.3 Characterisation of the coupler

The coupling was characterised using the Keysight E4990A-120 impedance bridge. The results shown in Table 1 compare the characteristic values L_1 , L_2 and M between the measurement, simulation, and FEM results.

The measurements are very close to the simulations for the primary. Nevertheless, some differences are observed for the secondary (+15%) that can be explained by the additional length of the wire planned to change the number of turns. For the chosen operating point ($D = 21$ cm), the error on the mutual is -8%. By recording the frequency of off-load impedance for the coupler alone, seen from the primary, between 1 kHz and 10 MHz, the first parasitic resonance at frequency of 580 kHz is observed, as shown in Fig. 9.

5 Design and fabrication of converter

5.1 Selection of the compensation elements

The compensation capacitors are determined considering the coupler self-inductances and the resonance frequency, which is less than the working frequency of 85 kHz. For a resonance frequency of 80 kHz, the selected values are as follows:

$$\begin{aligned} C_1 &= 12.5 \text{ nF}, & V_{C1\text{rms}} &\sim 5.3 \text{ kV} \\ C_2 &= 50 \text{ nF}, & V_{C2\text{rms}} &\sim 2.2 \text{ kV} \end{aligned}$$

These values are realised with unit capacitors of 100 nF/1000 V (CELEM) according to the following arrangement:

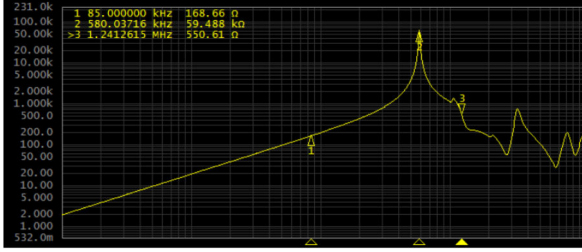
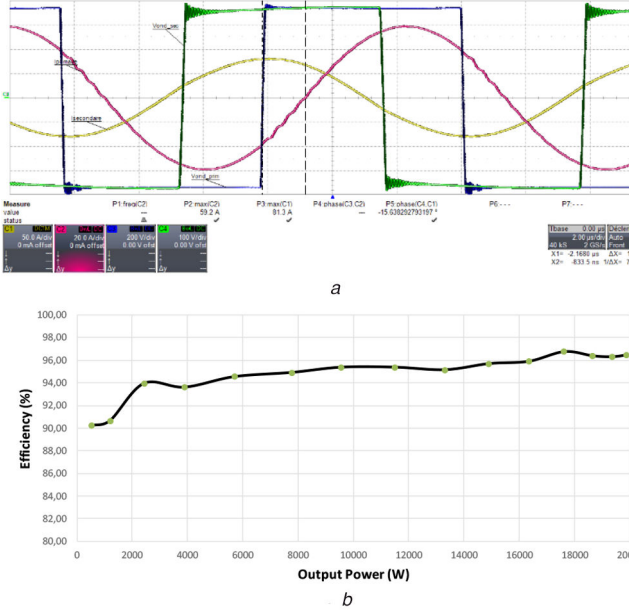
- C_1 : Eight capacitors in series.
- C_2 : Four sets of two capacitors in series.

5.2 Fabrication of bridge inverter

The input and output inverters, which the primary one is shown in Fig. 8b, are based on a standard two-level SiC 1200 V transistor structure (Microsemi APTMC120AM55CT1AG modules for the primary and APTMC120AM20CT1AG for the secondary). Two polypropylene capacitors in parallel with a unit value of 14 μ F are

Table 1 Comparison measurement/simulation

$N_1 = 23$ turns, $N_2 = 12$ turns		L_1 , μH	L_2 , μH	M , μH
$D = 14$ cm	measurement	316,15	75,17	38,79
	Ana. model	309,21	63,4	42,28
	3D FEM	314,2	69,33	39,02
$D = 21$ cm	measurement	315,81	73,53	21,13
	Ana. model	316,78	64,15	22,95
	3D FEM	315,73	68,12	21,62

**Fig. 9** Primary off-line impedance**Fig. 10** Output characteristics of the charger

(a) Waveforms at nominal power (blue line: v_1 (200 V/div), red line: i_1 (20 A/div), green line: v_2 (100 V/div), yellow line: i_2 (50 A/div)), (b) The converter efficiency

used to compose the DC bus capacitor of the inverter. Each power switch is controlled by a gate drive circuit, fabricated by an opto-coupler, a single gate driver (UCC27531) and a floating power supply of +20 V/−5 V (MGJ2D242005SC). Both converters are cooled by a water plate (ATS-CP1002). The entire structure is driven by an Field Programmable Gate Array (FPGA) (Altera Cyclone IV).

5.3 Experimental results

The first tests in low power quickly revealed problems of voltage withstand of the coupler. Isolation distances between turns and magnetic core had to be increased (up to 2 mm), especially for the coupler supply wires and the secondary in contact with the magnetic circuit.

The bus voltages are 750 V for the primary and 450 V for the secondary and the two inverters operate in the vicinity of 81 kHz. The power variation is ensured by the phase shift between the primary and secondary inverters. Fig. 10a shows the experimental voltage and current of the system at nominal power (20 kW delivered to the battery in charger mode). The efficiency curve of

the entire structure as a function of power is given in Fig. 10b. This efficiency reaches 96.45% at rated power.

6 Reversible V2G operation

6.1 Modelling

Reversibility of the power can be realised by the two inverter bridges and controlled by the phase shift between their controllers. Fig. 11a represents the three-inductor model with compensation of a DAB. This model has the advantage of showing a perfect coupler whose transformation ratio is equal to the ratio of the turns number. The relations between the elements of this scheme as well as the elements L_1 and L_2 and M are explained as:

$$L_{F1} = (1 - k_1)L_1 \text{ with } k_1 = \frac{1}{m} \frac{M}{L_1} \quad (23)$$

$$L_{F2} = (1 - k_2) \frac{L_2}{m^2} \text{ with } k_2 = m \frac{M}{L_2} \quad (24)$$

$$L_M = k_1 L_1 = k_2 \frac{L_2}{m^2} \quad (25)$$

$$k = \frac{M}{\sqrt{L_1 L_2}} = \sqrt{k_1 k_2} \quad (26)$$

It should be noted that in the presence of a symmetrical magnetic system (identical primary and secondary geometries), the coupling coefficients k_1 and k_2 would be equal and consequently $L_{F1} = L_{F2}$.

Elements of the T-model shown in Fig. 11b are explained in the sinusoidal mode as:

$$\underline{Z}_{T1} = \frac{1 - (1 - k_1)L_1 C_1 \omega^2}{j C_1 \omega} \quad (27)$$

$$\underline{Z}_{T2} = \frac{1 - (1 - k_2)L_2 C_2 \omega^2}{j m^2 C_2 \omega} \quad (28)$$

$$\underline{Z}_{TM} = j k_1 L_1 \omega \quad (29)$$

This scheme can be transformed to Π to explain the series impedance (denoted as Z) between the inverters, as shown in Fig. 11c. With Kennelly's transformation, one can deduce the expression of Z as follows:

$$\underline{Z} = \underline{Z}_{T1} + \underline{Z}_{T2} + \frac{\underline{Z}_{T1} \underline{Z}_{T2}}{\underline{Z}_{TM}} \quad (30)$$

This impedance is expressed at resonance by

$$\underline{Z} = -j k_1 L_1 \omega_R = -j \frac{M}{m} \omega_R \quad (31)$$

Impedance Z will allow one to reuse the main results of the DAB, in particular the expression of the power which is a function of the phase difference between the input and output bridges. However, given the negative nature of this impedance, the sense of transfer will be opposed to that of a conventional DAB with link inductance. The transferred power will then be expressed by the following formula:

$$P_o = \frac{|\underline{V}_1| |\underline{V}_2/m| \sin(-\varphi)}{|\underline{Z}|} = \frac{|\underline{V}_1| |\underline{V}_2| \sin(-\varphi)}{M \omega_R} \quad (32)$$

in which P_o is the power supplied to the battery and φ is the delay of the secondary bridge with respect to the primary bridge. Therefore, it is necessary to impose an advance phase ($\varphi < 0$) for the charger mode and a reverse phase for the mode in which the power is transferred from the battery to the network (V2G). In this work, it is found that the power is inversely proportional to

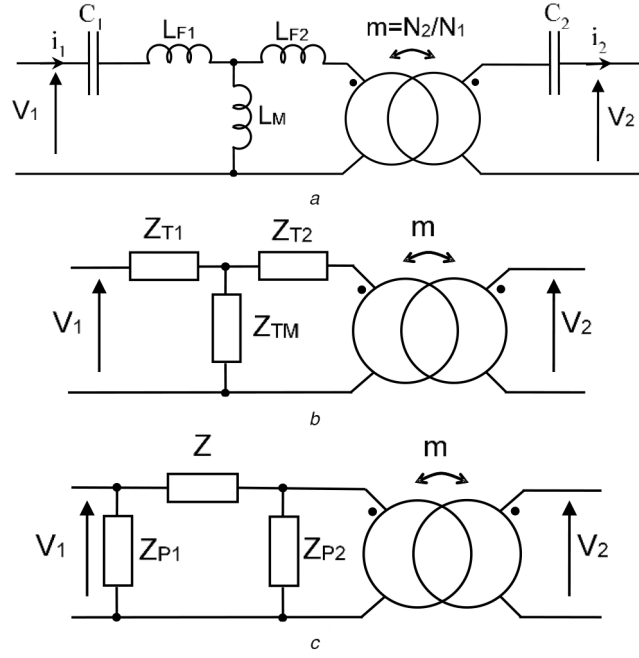


Fig. 11 Different types of equivalent circuits

(a) Equivalent circuit with compensation, (b) T model equivalent circuit, (c) Pi model equivalent circuit

impedance of the mutual inductance M ($M\omega_R$), as for currents I_1 and I_2 .

6.2 Control principle

The phase shift control (φ) allows the control of the power at given frequencies and voltages. The power is between +20 kW (charger) and -20 kW (V2G mode) for a frequency set at the resonant frequency. The power variation was obtained per action on φ , by (32), as shown in Fig. 12b:

$$\begin{aligned}\varphi < 0 &\rightarrow \text{G2V}, \\ \varphi > 0 &\rightarrow \text{V2G}.\end{aligned}$$

In practice, through their own gate driver, each power Metal Oxide Semiconductor Field Effect Transistor (MOSFET) of the whole structure is wire connected to the DE0-Nano board (FPGA Altera cyclone IV – EP4CE22F17C6N). At fixed frequency and voltage, a look-up table with several phase shifts between the primary and secondary inverters is implanted to FPGA. Thanks to this table, the transferring power from the G2V or V2G could be adjusted. Tests have been done in the open loop to increase or decrease the power and to choose between the G2V or V2G modes.

It is again checked for this frequency that the primary and secondary currents are independent of the phase shift φ and are directly related to the input and output voltages. Minimising variable power currents, especially when switching from one mode to another, will require the use of controlling α_1 , α_2 of each inverter. In order to guarantee the ZVS mode on each of them, the control of the duty cycle must be related to the phase shift φ . Fig. 12a shows the waveforms for the duty cycles α_1 , α_2 of each inverter. The respective phases of the primary (φ_1) and secondary (φ_2) currents correspond to the ZVS mode in this figure. Switching conditions in the ZVS mode for each inverter are dictated by the sign of the output current of each leg ($+i_1$ or $-i_2$), which should be opposite to the sign of the derivative switching inverter voltage (V_{a1} or V_{a2}):

$$\begin{aligned}+I_1 &\text{ should be lagged with respect to } V_{a1}, \\ -I_1 &\text{ should be lagged with respect to } V_{a2} \text{ (Fig. 13)}.\end{aligned}$$

This condition leads to the following relations on the phases φ_1 and φ_2 :

$$(1 - 2\alpha_1)\frac{\pi}{2} < \varphi_1 < (1 + 2\alpha_1)\frac{\pi}{2} \quad (33)$$

$$(1 - 2\alpha_2)\frac{\pi}{2} < -\varphi_2 < (1 + 2\alpha_2)\frac{\pi}{2} \quad (34)$$

Expressions (10) and (11) also make it possible to express the relations between the phases of the currents and controlled phase φ , at the resonant frequency as follows:

$$\varphi_1 = \frac{\pi}{2} + \varphi \quad (35)$$

$$\varphi_2 = -\left(\frac{\pi}{2} + \varphi\right) \quad (36)$$

By replacing these expressions in inequalities (33) and (34), we obtain the conditions on the minimal duty cycles in order to guarantee the ZVS mode as

$$\alpha_1 > \frac{|\varphi|}{\pi} \quad (37)$$

$$\alpha_2 > \frac{|\varphi|}{\pi} \quad (38)$$

Fig. 12b shows an example of evolution of the duty cycle guaranteeing the ZVS mode during the variation of the phase shift φ (power variation or start of the converter). Given (37) and (38), duty cycles α_1 , α_2 are chosen to be greater than the theoretical minimum in order to guarantee a sufficient phase margin for the both inverters (φ_1 and φ_2 are between 0 and 28° at full power). The power and currents are obtained in actual conditions, as shown in Figs. 12b and c, respectively. Tuning of the primary and secondary resonant frequencies could not be perfect in this case. The working frequency 81.474 kHz is then chosen at a value close to resonance (80 kHz) to ensure sufficient phase margins.

Experimental waveforms in V2G mode are shown in Fig. 12d. These results correspond to the conditions of Fig. 12b for a phase shift φ of 30° ($P_0 = 7.25$ kW). The conditions are as follows:

Primary: DC bus at $V_i = 750$ V, $I_1 = 38.5$ A, $\alpha_1 = 0.25$.

Secondary: Batteries at $V_o = 400$ V, $I_2 = 40$ A, $\alpha_2 = 0.39$.

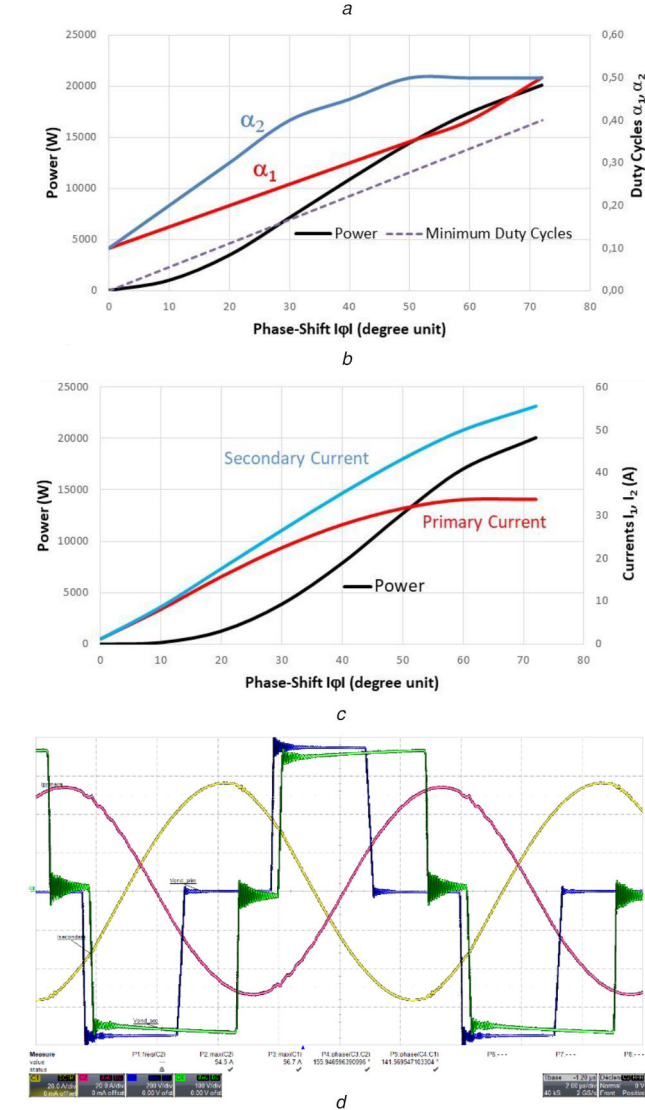
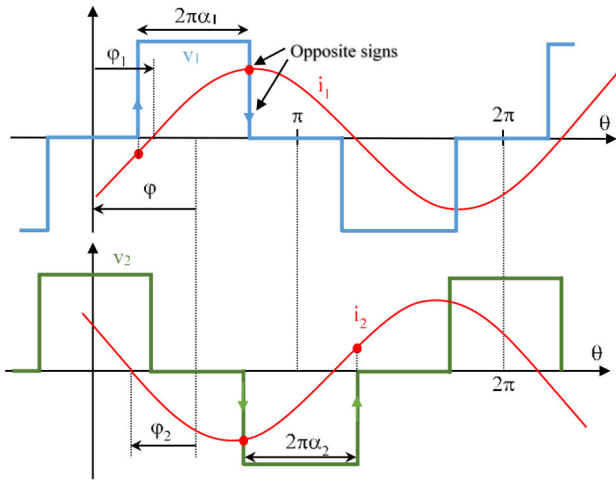


Fig. 12 The inverter waveforms

(a) Voltages and duty cycles for each inverter, (b) Variation of duty cycle and transferred power versus phase shift, (c) Primary and secondary currents and transferred power versus phase shift, (d) Experimental results in V2G mode (blue line: v_1 (200 V/div), red line: i_1 (20 A/div), green line: v_2 (100 V/div), yellow line: i_2 (20 A/div))

One can observe the smooth operation with sufficient phase margins of the system from these results.

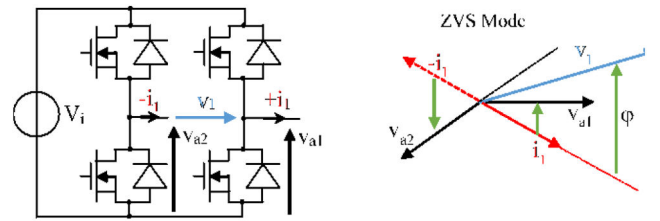


Fig. 13 Definition of the switching inverter voltages and the corresponding phasor diagram

7 Conclusion

An analytical model for the proposed contactless charger was presented, by which the transfer charging power and V2G power are controlled to be as high as possible. The system is controlled using the analytical model to transfer the maximum power in the first stage. Then, the system specifications are readjusted by a finite-element model, as a fine tuning. The soft switching in both the charging and regenerative modes was fulfilled. The system was assessed in detail theoretically. Using a prototype in 20 kW, simulation results and performance of the proposed system were confirmed in practice.

8 Acknowledgments

This work has been supported by the French Ministry of foreign affairs and the ministry of research and higher education and also the Iranian Ministry of science, research and technology within the frame of Gundishapur program.

9 References

- [1] Li, S., Mi, C.C.: 'Wireless power transfer for electric vehicle applications', *IEEE J. Emerging Sel. Top. Power Electron.*, 2015, **3**, (1), pp. 4–17
- [2] Choi, S.Y., Gu, B.W., Jeong, S.Y., *et al.*: 'Advances in wireless power transfer systems for roadway-powered electric vehicles', *IEEE J. Emerging Sel. Top. Power Electron.*, 2015, **3**, (1), pp. 18–36
- [3] Rim, C.T., Mi, C.: 'Wireless power transfer for electric vehicles and mobile devices' (Wiley-IEEE Press, New Jersey, USA, 2017)
- [4] Bi, Z., Kan, T., Mi, C.C., *et al.*: 'A review of wireless power transfer for electric vehicles: prospects to enhance sustainable mobility', *Appl. Energy*, 2016, **179**, pp. 413–425
- [5] Musavi, F., Eberle, W.: 'Overview of wireless power transfer technologies for electric vehicle battery charging', *IET Power Electron.*, 2014, **7**, (7), pp. 60–66
- [6] Daga, A., Miller, J.M., Long, B.R., *et al.*: 'Electric fuel pumps for wireless power transfer', *IEEE Power Electron. Mag.*, 2017, **4**, (2), pp. 24–35
- [7] Na, K., Jang, H., Ma, H., *et al.*: 'Tracking optimal efficiency of magnetic resonance wireless power transfer system for biomedical capsule endoscopy', *IEEE Trans. Microw. Theory Tech.*, 2015, **63**, pp. 295–304
- [8] Ahn, D., Ghovanloo, M.: 'Optimal design of wireless power transmission links for millimeter-sized biomedical implants', *IEEE Trans. Biomed. Circuits Syst.*, 2016, **10**, pp. 125–137
- [9] Sampath, J.P.K., Alphones, A., Vilathgamuwa, D.M.: 'Figure of merit for the optimization of wireless power transfer system against misalignment tolerance', *IEEE Trans. Power Electron.*, 2017, **32**, (6), pp. 4359–4369
- [10] Hou, J., Chen, Q., Wong, S.C., *et al.*: 'Analysis and control of series/seriesparallel compensated resonant converters for contactless power transfer', *IEEE J. Emerging Sel. Top. Power Electron.*, 2015, **3**, (1), pp. 124–136
- [11] Feng, H., Duan, S., Zhao, J.: 'An LCC-compensated resonant converter optimized for robust reaction to large coupling variation in dynamic wireless power transfer', *IEEE Trans. Ind. Electron.*, 2016, **63**, (10), pp. 6591–6601
- [12] Yin, J., Lin, D., Parisini, T., *et al.*: 'Front-end monitoring of the mutual inductance and load resistance in a series-series compensated wireless power transfer system', *IEEE Trans. Power Electron.*, 2016, **31**, (10), pp. 7339–7352
- [13] Zhang, W., Mi, C.C.: 'Compensation topologies of high-power wireless power transfer systems', *IEEE Trans. Veh. Technol.*, 2016, **65**, (6), pp. 4768–4778
- [14] Zhu, Q., Wang, L., Liao, C., *et al.*: 'Improving the misalignment tolerance of wireless charging system by optimizing the compensate-capacitor', *IEEE Trans. Ind. Electron.*, 2015, **62**, (8), pp. 4832–4836
- [15] Liu, D., Hu, H., Georgakopoulos, S.V.: 'Misalignment sensitivity of strongly coupled wireless power transfer systems', *IEEE Trans. Power Electron.*, 2017, **32**, (7), pp. 5509–5519
- [16] 'Wireless power transfer for light-duty plug-in/electric vehicles and alignment methodology', norm SAE J 2954, 2017